Nanoscale Advances

ROYAL SOCIETY OF CHEMISTRY

PAPER

View Article Online
View Journal | View Issue

Cite this: *Nanoscale Adv.*, 2025, **7**, 2648

Metal–ligand interface effect in the chirality transfer from L- and D-glutathione to gold, silver and copper nanoparticles†

Juan Carlos López-Olivos, [a] Andrés Álvarez-García, [a] Georgina Garza Ramos,[b] Lázaro Huerta,[c] Paola Molina,[d] Alejandro Heredia-Barbero, [d] Ignacio L. Garzón [ae] and Penélope Rodríguez-Zamora *[a]

Glutathione (GSH) plays a pivotal role in numerous physiological and metabolic processes, including the defense of cells against free radicals and metal toxicity. This tripeptide has been combined with several metal nanoparticles to form a metal–organic interface with unique properties. Here, we implement a one-step, high-yield synthesis method to produce ultrasmall gold, silver, and copper nanoparticles in the intermediate size regime between size-selected nanoclusters and plasmonic nanoparticles to be functionalized with L- and D-glutathione, and study the chirality transfer evidenced by the emergent optical activity observed for each case. The distinctive interactions that take place at the metal–ligand interface for each metal are primarily accountable for establishing the properties of this system. In its protonated state, glutathione anchors only by its thiol group to the surface of gold and copper nanoparticles, whilst for silver nanoparticles an additional binding site through the nitrogen atom of the amide group was indicated by XPS data, albeit with a relatively low proportion. This may contribute to the higher anisotropy factor observed in silver–glutathione nanoparticles. Such slight variations in adsorption configuration generate different chiroptical activity, which has been analyzed per energy region using time-dependent DFT calculations, revealing that metal-to-ligand transitions dominate most of the spectra while ligand-to-ligand are also present in the higher energy regime. Moreover, FTIR and CD data together suggest that those dissimilarities also propitiate particular peptide self-assemblies through intermolecular GSH interactions for each metal, which result in supramolecular structures with properties of beta-sheet arrays. This study offers a parallel examination of the chirality of glutathione-functionalized coinage metals, allowing to establish decisive differences that can be tailored to benefit developments in chiral biomedicine and other diverse applications.

Received 28th February 2025
Accepted 6th March 2025

DOI: 10.1039/d5na00208g

rsc.li/nanoscale-advances

1 Introduction

The functionalization of nanoparticles can be achieved through the addition of a chemical species to their surface, which can impart new optical, electronic, magnetic, and catalytic properties; promote self-organization; control their size; and make the nanoparticles compatible for a desired application, particularly in the context of biomedical developments.[1–6] Ultrasmall nanoparticles (NPs) of gold, silver and copper can be functionalized using crosslinkers with thiol groups capable of reacting with the metal and producing a covalent bond.[7–11] These bifunctional linkers have at the other end functional groups to use as binding ligands.[12–16]

Glutathione (GSH) is a naturally occurring tripeptide (γ-Glu-Cys-Gly) and serves as an important example of a nanoparticle capping ligand.[5,9,15,17–19] GSH bears intrinsic metal-chelating properties due to the presence of a thiol group in its molecular structure, which allows the formation of high-affinity metal–ligand clusters.[20] This tripeptide is abundant in the cytoplasm and has a multitude of physiological functions, such as redox buffering, detoxification, and antioxidant activity,[21,22] properties that are maintained when this molecule is conjugated with metal NPs.[5,23–26] Presumably, the special properties of the GSH-functionalized NPs stem at least partially from the multiple possibilities available for intermolecular hydrogen

[a]*Instituto de Física, Universidad Nacional Autónoma de México, Apartado Postal 20-364, Ciudad de México 01000, Mexico. E-mail: penelope@fisica.unam.mx*
[b]*Facultad de Medicina, Universidad Nacional Autónoma de México, Av. Universidad 3000, Ciudad de México 04510, Mexico*
[c]*Instituto de Investigación en Materiales, Universidad Nacional Autónoma de México, Circuito Exterior S/N, Circuito de la Investigación Científica 04510, Ciudad de México 04510, Mexico*
[d]*Instituto de Ciencias Nucleares, Universidad Nacional Autónoma de México, Circuito Exterior S/N, Ciudad Universitaria, Apartado Postal 70-543, C.P. 04510, Mexico*
[e]*Departamento de Física Teórica, Atómica y Óptica, Universidad de Valladolid, E-47011 Valladolid, Spain*

† Electronic supplementary information (ESI) available. See DOI: https://doi.org/10.1039/d5na00208g

bonding in GSH, allowing for the formation of varying molecular self-assemblies propitiated by the metal–ligand interactions.[12,27,28]

Among all the research and applications in current development of the multiple physiological functions of metal nanoparticles functionalized with glutathione, there is one special property that has just started to be explored in the biomedical area: their chirality.[29–31]

In general, chiral inorganic nanomaterials with biomedical applications have become a popular research field during the last decades, ranging from ultrasensitive detection and imaging to therapeutic purposes.[1,32–36] Recently it has been demonstrated that nanoparticle chirality can influence the immune response.[35,36] By synthesizing gold nanoparticles in the presence of circularly polarized light and a thiolate dipeptide (cysteine–phenylalanine),[34] Xu *et al.* achieved enantiospecific activation of immune cells, making them functional as adjuvants for vaccination against the H9N2 influenza virus.

In particular, the chirality and other properties of glutathione, such as its anti-oxidative function, have been combined with metal nanoparticles to incide into neurodegenerative diseases such as Parkinson and Alzheimer.[36–39] The uptake of GSH-functionalized NPs by cancer cells also makes them an efficient drug-delivery agent.[15,30] These examples exhibit the relevance of achieving a profound understanding of the synergy emergent from conjugating metal nanoparticles with glutathione, specifically in terms of their chirality.

Such understanding started more than 20 years ago, when chiroptical activity was detected for glutathione-functionalized gold nanoclusters,[40,41] showing discrete electronic transitions between quantized levels, each associated with a delocalized orbital of the conduction band[41–43] resulting in a strong optical activity. Since then, many works have focused attention on metal nanoclusters and nanoparticles conjugated with glutathione, given the varied properties that exhibit which are totally absent in the bulk.[44–48]

Throughout many studies, the unveiling of the mechanisms concerning the adsorption configuration of this ligand on different metal nanoparticles and the origin of the chirality of these hybrid nanosystems has been of particular relevance.[8,12,38,43,49–52] Similarly to other thiol-functionalized metal nanoparticles, the ligand–metal interface plays a crucial role in the chiral properties of nanoparticles functionalized by GSH.[7,42,53–57]

Chiral ligand-induced effects on the electronic structure and chiroptical properties of ultrasmall GSH-functionalized metal NPs (especially gold) had long been studied from different angles given the difficulties that the inherent flexibility of this molecular ligand represent.[58–60] Those characteristics have been partly the cause for not having an atomic structural determination of metal-GSH (Met-GSH) nanoclusters[47,49,61] in contrast with a considerable number of thiol-functionalized metal nanoclusters that have been determined to the date.[43,62,63] However, precise chemical formulas of several sizes $[Au_n(SG)_m]$ of Au-GSH nanoclusters have been unambiguously identified based on high-resolution mass spectroscopy experiments from 2005 to 2007, and chiro-optically characterized,[6,41,44,45,48,64,65] from which significant experimental[3,17,46,66–68] and theoretical[50,69] progress has been made in determining how the metal–ligand interface and ligand dynamics are important for the structural and electronic properties of the clusters. As the size of the gold core is reduced to below 2 nm, the attachment of thiolates to these ultra-small clusters has a marked effect on their geometric structures and electronic properties. This observation indicates that the formation of Au–S bonds plays a significant role in determining the structures and characteristics of the binary system.[70]

Extending this analysis to other metal nanoparticles such as silver and copper, it has also been demonstrated that the nature of the metal defines the chirality of the whole Met-ligand system.[71] Gold, silver and copper, also known as the coinage metals, are the members of the group 11 in the periodic table given their shared electron configuration patterns, principally in the outermost shells, resulting in trends in chemical behavior. Despite these similarities, when conjugated with thiolate ligands, each metal exhibits unique adsorption configuration structures, owing to the differences in metal–sulfur bonding.[72] Some theoretical comparisons of the three metals have been reported in terms of the nature of their bond with thiolate molecules. For example, Kacprzak *et al.*[73] ascertained the Cu–S bond as the strongest and most polar among the three metals, and Au–S bond as the most covalent. More recent studies[74] confirm gold as the king of stable ligand–metal complexes and clusters but places copper in a closed second place, highlighting the interesting charge-transfer properties of Cu–S; and depict Ag–S as a balanced intermediate between gold and copper for holding the structural integrity and molecular composition of metal–thiolate systems.

The metal–thiolate binding will also determine what functional groups are available to interact with adjacent molecules and therefore which supra-assemblies are feasible given the rearrangement of the hydrogen-bonding network within the adsorbed layer.[12,66,75,76]

Depending on the synthesis method implemented, it is possible to observe different manifestations of chirality transfer between glutathione and metal NPs,[77,78] varying from the extensively studied thiol-functionalized nanoclusters[44,47,48] to other structures such as ultrasmall catenane clusters[65,79] and large oligomeric Au(I)–thiolate complexes.[80,81]

In the present work we used microwave assisted hydrolysis to synthesize ultrasmall gold, silver and copper nanoparticles ($\leq$2 nm) in order to functionalize them with L-GSH (γ-L-glutamyl-L-cysteinyl-glycine) and its optical isomer, D-GSH (*N*-γ-D-glutamyl-D-cysteinyl-glycine).[24] It is our understanding that this is the first systematic comparison of gold, silver and copper nanoparticles in the intermediate size range between metal nanoclusters (dozens of atoms) and larger plasmonic NPs (>2 nm) functionalized with both glutathione enantiomers. The observed optical and chiroptical behaviour are contrasted with small GSH-protected clusters on one hand,[3,41,44,45,47,82] and previously reported results from nanoparticles of the same size also produced by microwave assisted hydrolysis, functionalized with cysteine[71] on the other.

Both enantiomeric Met-LGSH and Met-DGSH nanoparticles of each metal were characterized by transmission electron microscopy (TEM), Fourier transform infrared spectroscopy (FTIR), X-ray photoelectron spectroscopy (XPS), UV-Vis spectroscopy and circular dichroism spectroscopy (CD). In all three cases it was found a chirality transfer from the molecular ligand to the Met-GSH conjugate, evidenced by mirror CD spectra which showed a distinctive spectrum for each metal. A time-dependent density functional theory analysis was also performed on Met-GSH motifs to portray the electronic transitions responsible for the emergence of their chiroptical absorption.

This one-step green synthesis method is considerably easier and faster compared to previously reported laborious techniques for the synthesis of atomically precise thiol-protected nanoclusters, and therefore a competitive and effective route for the high yield of chiral metal–ligand nanoparticles required by biomedical applications that may not demand accuracy in the number of atoms.

2 Methodology

2.1 Experimental details

Synthesis of metal nanoparticles. Tetrachloroauric acid ($HAuCl_4 \cdot 3H_2O$, ≤99.9%), silver nitrate ($AgNO_3$, 99.5%), and hydrated copper nitrate ($Cu(NO_3)_2 \cdot 3H_2O$, 99.5%) were purchased from Sigma-Aldrich and used without further purification. Gold (Au NP), silver (Ag NP) and copper nanoparticles (Cu NP) were synthesized by microwave-assisted hydrolysis according to a previously reported method with some modifications.[83,84] To prepare bare Au, Ag and Cu NP, the respective metal precursors were dissolved in deionized water to obtain 5 mM of $HAuCl_4$, $AgNO_3$ and $Cu(NO_3)_2$, respectively. Each solution is then irradiated at 1000 W for 10 s using a commercial microwave system and let to cool at room temperature.

Preparation of glutathione functionalized metal nanoparticles. L-Glutathione was purchased from Sigma-Aldrich, while D-glutathione was obtained from GL Biochem (Shanghai) Ltd. In order to prepare glutathione-functionalized gold, silver and copper nanoparticles (Au-GSH, Ag-GSH and Cu-GSH respectively), in each case, the peptide was directly dissolved in solutions of Au, Ag, and Cu nanoparticles to achieve a concentration of 25 mM. The nanoparticles were precipitated by adding ethanol, effectively removing excess thiol and other by-products.

Samples characterization. Transmission electron microscopy (TEM) images were acquired using a JEOL ARM200F Cs-aberration-corrected electron microscope operating at 80 kV. The imaging was performed through scanning transmission electron microscopy (STEM) with high-angle annular dark field (HAADF) detection.

X-ray photoelectron spectroscopy analyses were carried out in an ultra-high vacuum (UHV) system scanning XPS microprobe PHI 5000 VersaProbe II, with an Al Kα X-ray source ($h\nu$ = 1486.6 eV) monochromatic with 200 μm beam diameter, and a Multi-Channel Detector (MCD) analyzer. The samples surface was etched for 5 min with 1 kV Ar^+ at 0.11 μA mm^{-2}. The XPS spectra were obtained at 45° to the normal surface with Constant Analyzing Energy (CAE) E_0 = 117.40 and 11.75 eV survey surface and high-resolution narrow scan. The peak positions were referenced to the background Ag $3d_{5/2}$ photopeak at 368.20 eV, with an FWHM of 0.65 eV, and C 1s hydrocarbon groups at 285.00 eV, Au $4f_{7/2}$ at 84.00 eV central peak core level position. The XPS spectrum was fitted with the program Multipack® PHI Software[85] and Spectral Data Processor, SDP v 4.1.[86]

FT-IR spectra were recorded using a Bruker VERTEX 70 FT-IR spectrometer over a range of 600–4000 cm^{-1}, with a resolution of 2 cm^{-1} and phase accumulation of 32 or 64 scans. All spectra were collected using liquid samples. UV-Vis absorption spectra were measured with a Thermo Scientific UV-Vis Evolution 201 spectrophotometer. Electronic circular dichroism (CD) spectra were obtained using a Chirascan spectropolarimeter (Applied Photophysics, Leatherhead, Surrey, UK) equipped with a Peltier-type cell holder. All UV-Vis absorption and CD spectra were collected using a quartz cuvette with a 1 cm path length.

2.2 Computational details

The staple motif was employed as a model for the interface of GSH-protected nanoparticles.[43] This model comprises two metal atoms, which represent the nanoparticles, and an additional metal atom that serves to bridge two glutathione molecules.[71] Au-GSH, Ag-GSH, and Cu-GSH motifs were optimized using the Orca 5.0.3 code at the density functional theory (DFT) level.[87,88] All relaxations were performed employing the hybrid PBE0 exchange–correlation functional with a restricted Kohn–Sham formalism.[89,90] Glutathione (GSH) atoms were treated with the TZVP basis set,[91] while the metal atoms were treated using the Zero Order Regular Approximation (ZORA) to account for scalar relativistic effects.[92,93] The solvent effect (water) was taken into account by the conductor-like polarizable continuum model (CPCM) in an infinite dielectric and with a Gaussian charge scheme.[94] Time-dependent density functional theory (TD-DFT) calculations of the oscillator and rotatory strengths were performed considering the first 300 excitation states. Natural transition orbitals (NTOs) were calculated to analyze the excited states. NTOs diagonalize the transition density matrix (TDM) similarly to how natural orbitals serve as the eigenfunctions of the density matrix. They represent a unitary transformation of the canonical orbitals, thereby creating a set of electron–hole orbitals. This transformation offers a valuable means of qualitative analysis of electronic excitations.[95,96]

3 Results and discussion

3.1 Experimental results

Bare metal nanoparticles (Fig. S1†) were synthesized by microwave assisted hydrolysis, which allows for accelerated reduction reaction,[83,84] yielding a narrow size distribution without further purification.

Differently from other gold–glutathione NPs synthesis methodologies reported previously,[18,41,44,45,80,97,98] which start with conjugation of $HAuCl_4$ with glutathione, generating oligomeric Au(I)–thiolate complexes or glutathione–Au(I) polymers,

that subsequently are reduced by $NaBH_4$ and size selected by electrophoresis, microwave assisted hydrolysis promotes formation of a dominant population of ultrasmall metal nanoparticles that are subsequently functionalized by glutathione which acts both as a reducing agent and a ligand that stops further nucleation.[20,80,81,99] The process results in Met(0) Met(I)–thiolate nanoparticles (Met = Au, Ag, Cu) with size distribution centered at 2 nm for silver and copper nanoparticles and at a slightly smaller diameter for gold nanoparticles, that can be clearly differentiated in STEM topographies (Fig. 1), and confirmed by FTIR spectroscopy, X-ray photoelectron spectroscopy and absorption spectrophotometry, as detailed below.

3.1.1 FTIR. Fig. 2 shows FTIR spectra of free L-GSH (Fig. 2a) and D-GSH (Fig. 2e) as well as Au, Ag and Cu NPs functionalized by L-GSH (Fig. 2b–d) and D-GSH (Fig. 2f–h). Adsorption of glutathione through its thiol group to the surface of the metal nanoparticles was confirmed by the absence of the S–H vibration band 2520 cm^{-1} in the FTIR spectrum of each Met-GSH NPs case (Fig. 2b–d and f–h).

FTIR spectra of L-GSH and D-GSH present slight variations between each other due to their crystalline polymorphism (whilst L-GSH is alpha, D-GSH is beta) as a consequence of their different synthesis routes (Fig. S2†). These crystalline polymorphs exhibit significant differences in their solubility in water,[100,101] which slightly influences their FTIR spectra when measured in aqueous solutions.

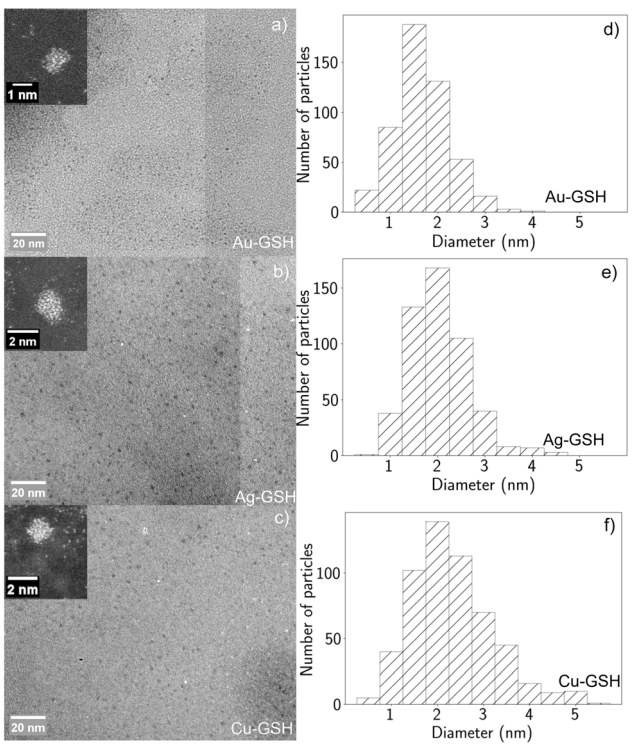

Fig. 1 Transmission electronic microscopy images of glutathione-functionalized metal nanoparticles Au-GSH (a); Ag-GSH (b); and Cu-GSH (c). Inset of a typical individual nanoparticle in each case. Size distributions for each corresponding case (d, e and f).

The ionic state of glutathione is determined by pH, consequently defining its anchoring sites on the metal surface, as well as the inter and intramolecular interactions, which are all interrelated factors involved in the interface configuration of the Met-GSH nanoparticles (intramolecular interactions dictate the molecular shape[66] and therefore the steric conditions of adsorption). In turn, all the mentioned factors, determine the molecular assembly propitiated by the presence of the metal nanoparticles which might involve a rearrangement of the hydrogen-bonding network formed on the surface of the metal nanoparticles.[28,66]

As expected from the acidic pH of our Met-GSH samples ($\leq$2.6 in all cases), which favors the cationic form of glutathione, the C–O–H bending mode is observed at 1130 cm^{-1} for Au-GSH; 1135 cm^{-1} for Ag-GSH; and at 1130 cm^{-1} for Cu-GSH for the left enantiomer (1130 cm^{-1} in all three cases for the right enantiomer), with higher intensity for all three metals compared to the free ligand spectrum.[66] Another feature is the band at 1394 cm^{-1} for Au-GSH; 1415 cm^{-1} for Ag-GSH; and 1389 cm^{-1} for Cu-GSH for both enantiomers, which is associated with the C–O–H stretching of the protonated GSH.[102] Such cationic conditions result in protonation of glutathione carboxyl terminals (with pK_a values of 2.4 ± 0.2 for COOH of glu and 3.6 ± 0.2 for COOH of gly[28,103–105]), inhibiting complexation with the metal surfaces of the nanoparticles.

Under these conditions, and taking into account that the isoelectric point of NH_3^+ is around 9.5, the most plausible scenario for the three metal nanoparticles is not having the carboxyl or amino functional groups as anchor sites in addition to the thiol group.[27,28,66,104,105] Thus, considering a preferred monodentate binding adsorption configuration of glutathione to the nanoparticle surface, the possibility of double hydrogen bonding between the glutamate of one glutathione with the glycine of another adjacent glutathione cannot be ruled out, which has been reported for pH $\leq$ 4.[27,28]

A region that has been previously analyzed with this respect corresponds to the amide I and II bands between 1500 and 1700 cm^{-1}. ATR-IR detailed studies[66] mention that weak signals were observed for the amide I region when, under acidic pH, the interaction of glutathione with Au NPs was given only through the thiol group. More recent studies,[81] have also analyzed this region (normally used to investigate protein secondary structure[106–108]) of free glutathione compared with glutathione as protective ligand of gold and silver nanoparticles, suggesting that this tripeptide tends to form beta-sheet-like structures when interacting with silver but not with gold nanoparticles, supporting their conclusion on a proposed double anchoring (through the thiol and carboxyl groups) of glutathione on Ag NPs and single on Au NPs. Within this region (Fig. 2i), our FTIR spectrum for free GSH shows bands at 1538 and 1589 cm^{-1} (amide II N–H bending and C–N stretching vibrations) and 1655 cm^{-1} (amide I C=O stretching). Au-GSH and Cu-GSH display a similar tendency throughout the region, whereas Ag-GSH exhibits a considerably diminished C–N str band, indicating a possible interaction between the peptidic nitrogen atom and the silver surface. On the other hand, transition at 1636, 1635 and 1641 cm^{-1} for Au-GSH, Ag-GSH and Cu-GSH

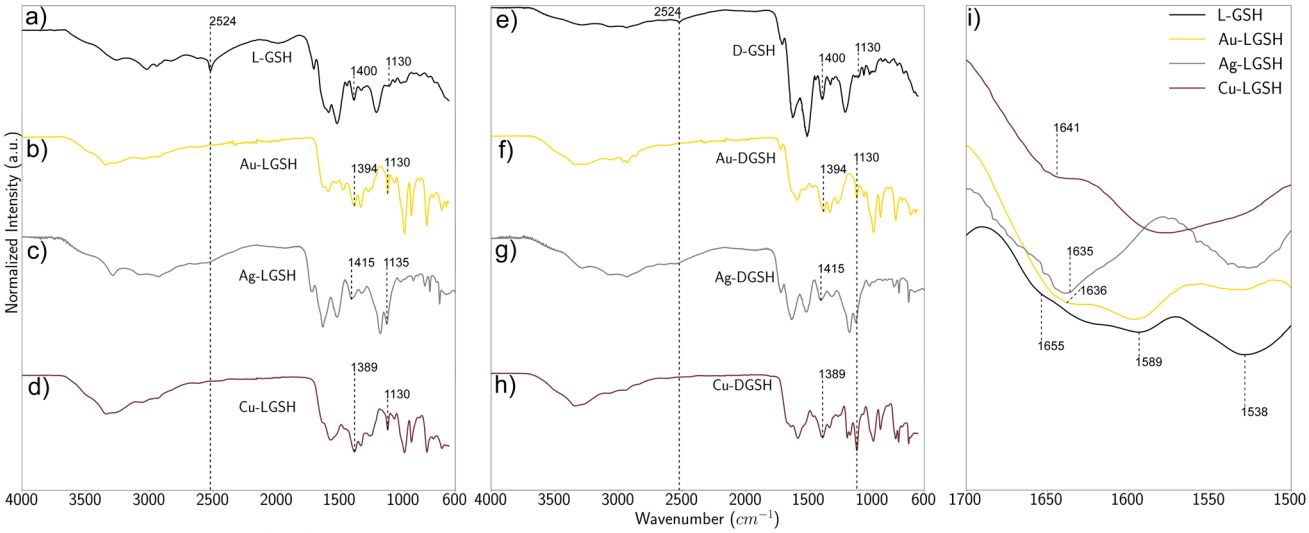

Fig. 2 Fourier transform IR spectroscopy of: (a) L-GSH, (b) Au-LGSH, (c) Ag-LGSH, (d) Cu-LGSH, (e) D-GSH, (f) Au-DGSH, (g) Ag-DGSH, (h) Cu-DGSH, and (i) the amide I and II region (1500 to 1700 cm^{-1}) for all Met-LGSH and L-GSH. The GSH S–H band can be observed in (a) and (e) at 2520 cm^{-1}, this band vanishes when glutathione is adsorbed on the surface of the metal nanoparticles (b–d and f–h).

respectively, is a characteristic feature of beta-sheet structure,[12,81,108] suggesting that the formation of an intermolecular array of glutathione enclosing the NPs might take place for all three metals. This result also suggests that the metal–ligand interface happening between gold and copper nanoparticles with glutathione is similar, particularly concerning the number of anchoring sites, and it does not drastically differ from the metal–ligand interaction in the case of silver nanoparticles.

Single or double anchoring would have repercussions on the molecular footprint and therefore on the number of ligands that can be adsorbed for same-size nanoparticles of different metals (NP–ligand ratio). If glutathione adsorbed by single binding (through S) on Au NPs and by double binding (through S and a second anchoring site) on Ag NPs, it could be anticipated that there would be more ligands on the surface of the former, given the steric restrictions imposed by a double anchoring. Recent studies[109] have approximated by different methods (inductively coupled plasma mass spectrometry ICP-MS, nuclear magnetic resonance NMR, elemental analysis (AAS and combustion analysis) EA and energy-dispersive X-ray spectroscopy EXD) the stoichiometry of glutathione functionalized gold and silver nanoparticles with an average diameter of 2 nm as well as the corresponding footprint for each case. According to this study, which is in agreement with earlier data on ultrasmall gold and silver nanoparticles,[10,110] the number of glutathione molecules adsorbed on the surface of gold and silver NPs fluctuates, depending on the technique, around the same value, and the molecular footprint also does not differ greatly from one metal to the other.

3.1.2 XPS. Our samples were subjected to X-ray photoelectron spectroscopy to further investigate the metal–ligand interface in GSH-functionalized metal NPs synthesized by microwave-assisted hydrolysis.

Photoemission spectra of glutathione and Met-GSH NPs were obtained by X-ray photoelectron spectroscopy (XPS) in order to elucidate the metal–organic interaction and quantify the known functional groups. C 1s, S 2p, N 1s, O 1s, Au 4f, Ag 3d, and Cu 2p core levels were analyzed by high-resolution spectra as shown in Fig. 3 and S3.† From comparison of C 1s (Fig. S3a†) and S 2p (Fig. 3b) orbitals corresponding to GSH with those corresponding to Met-GSH NPs, it is possible to identify the CH_2–SH and metal–S bonds, indicating that all three metal NPs coordinate with GSH by its thiol group, and that the tripeptide preserves its properties upon adsorption (of imperative importance for many biomedical applications[17,25,111]) with CH_2–S having the same BE of 286.55 eV in all samples.

The Au-GSH NPs spectrum showed elemental Au(0) and Au(I)–S with Au $4f_{7/2}$ and $4f_{5/2}$ peaks binding energies of 84.7 and 88.6 eV corresponding to a convolution of Au(0) species and a strong coordination of Au(I) with the ligand sulfur atoms (Fig. 3e). The blue-shifted position of Au($4f_{7/2}$) from Au(0) (Fig. 3e) and red-shifted from the Au(I)–thiolate compound (Fig. S4†), indicates the presence of two components originating from the inner (Au(0)) and surface (Au(I)) atoms of the gold NPs.[44,80] Glutathione S $2p_{3/2}$ peak at 163.77 eV (Fig. 3b) is a convolution of two curves corresponding to S–C for the free ligand, whereas for Au-GSH sample the S $2p_{3/2}$ BE is redshifted to 163.52 eV due to a convolution with Au–S core level at 162.30 eV. Note that a chemical shift in S 2p of 0.25 eV occurs when C–S bonds turn to the C–S–Met bonds in the presence of metal NPs.[112–114] The integral area ratio of Au–S bonds to total sulfur species is *ca.* 0.77, indicating that 77.3% of S present in the sample was coordinated with the Au atoms.[30] An electronic rearrangement throughout the system is given by charge transfer from the gold atoms of the NPs to GSH, where the sulfur atom, which is polar, accepts the charge but releases a hydrogen ion, producing an Au–S ionic bond; consistent with previous results.[44]

In the case of Ag-GSH NPs, the Ag $3d_{5/2}$ XPS spectrum showed a peak at 368.48 eV, very close to the energy for Ag(0), at

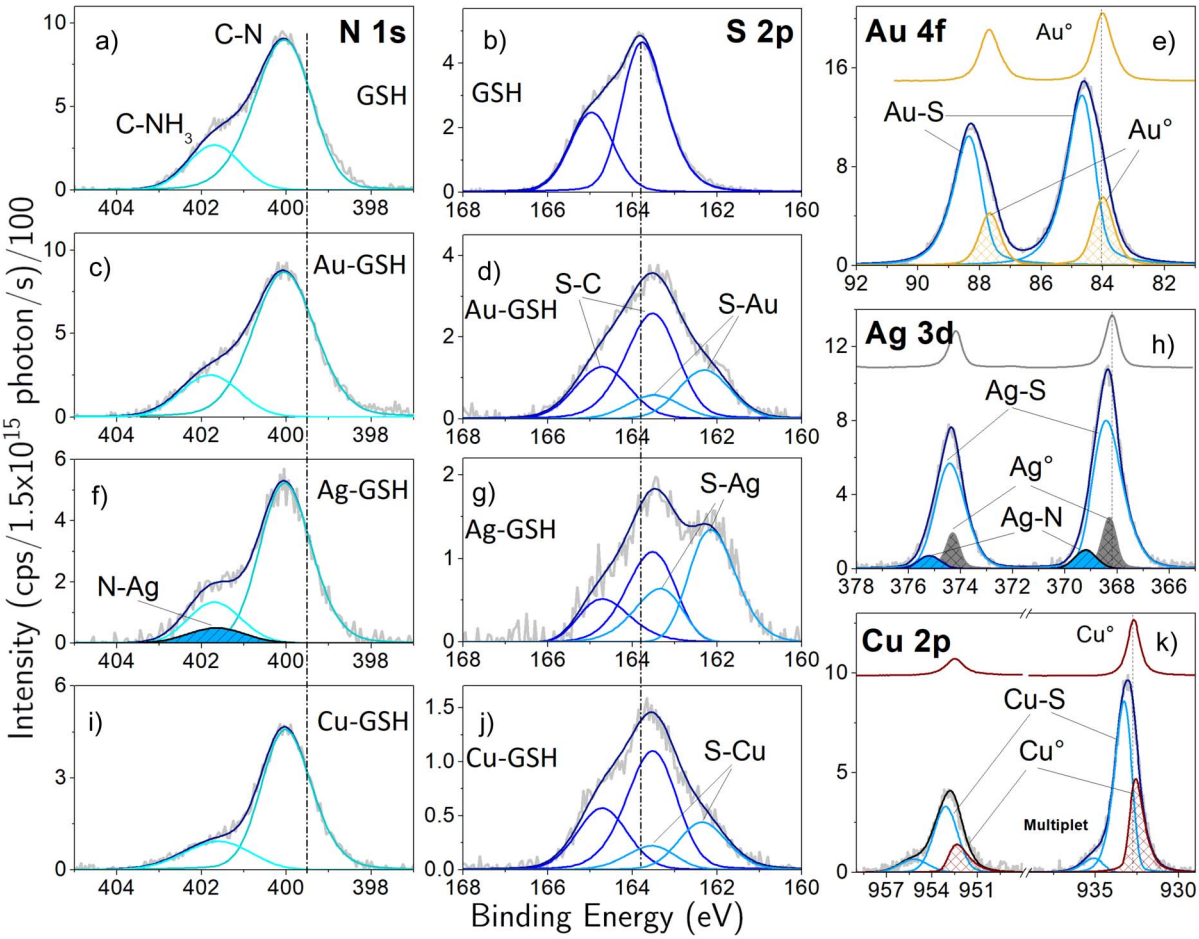

Fig. 3 High-resolution core level XPS deconvolution spectra of free GSH and GSH-functionalized metal nanoparticles. N 1s (a), (c), (f) and (i); S 2p (b), (d), (g) and (j); Au 4f (e); Ag 3d (h); and Cu 2p (k). At the top of (e), (h) and (k) simple orbitals of reference metals are shown. The deconvolution spectra show contributions of direct bonds of neighboring atoms. The S 2p and metal atom orbitals contain two oxidation states, as it can be seen in each doublet (spin–orbit).

368.30 eV, but slightly blue shifted due to Ag–S binding (Fig. 3h). Deconvolution of the S $2p_{3/2}$ peak in this case shows a much stronger contribution of Ag–S bonds compared to Au-GSH NPs, redshifting and generating a second peak at 162.15 eV (Fig. 3g). The integral area ratio of Ag–S bonds to sulfur species translates to 86% of the S atoms being coordinated with the Ag atoms, suggesting that glutathione actually has a stronger preference for binding to Ag NPs compared to Au NPs.

Finally, for Cu-GSH NPs, the binding energy for $Cu_2p_{3/2}$ is 933.6 eV, also blue-shifted from Cu(0) at 933.28 eV, and resulting from a convolution with Cu–S binding (Fig. 3i). Cu–S in $S_2p_{3/2}$ is at 162.35 eV (Fig. 3j) with a contribution from the sulfur species of 68.7%, being the lowest of the three metallic nanoparticles. The S_2p peak shows the lowest chemical shift (1.42 eV) with respect to the binding energy of free glutathione, compared to Au–S, which is shifted 1.47 eV and Ag–S with a chemical shift of 1.62 eV, this is consistent with the electronegativity of the NPs elements (1.90 for Cu, 1.93 for Ag and 2.54 for Au).

Regarding the discussion on anchoring sites, O 1s does not show peaks or possible contribution to convolution corresponding to Met-COO for any of the metals (Fig. 3b, d, f and h). On the other hand, for N 1s orbitals, Ag-GSH reveals a slightly different behavior compared to free GSH, Au-GSH and Cu-GSH (Fig. 3a, c, f and i), displaying a third contribution to the N 1s spectrum (of only 7.6%) with a peak at 401.65 eV, corresponding to a Ag–N bond. This result is consistent with the deconvolution of the Ag $3d_{5/2}$ spectrum (Fig. 3h), which shows a small peak at 369.2 eV associated with the Ag–N bond.

The above described findings suggest that, in general neither the carboxyl group nor the amino group function as second anchoring sites activated during synthesis *via* microwave assisted hydrolysis at acidic pH. This result differs with respect to cysteine-functionalized gold nanoparticles also synthesized by microwave assisted hydrolysis, for which one of the oxygens of the cysteine carboxyl group serves as second binding site.[115] Sterical hindrance seems to be the main reason for this important difference in metal–ligand interface structure: whilst cysteine's amino and carboxyl groups can both be in proximity to the metal surface for this size of metal nanoparticles, under

this conditions glutathione appears to preference a Y-shape which averts the functional groups from the vicinity of the nanoparticle surface.

However, in the case of silver nanoparticles a bidentate adsorption configuration of glutathione involving a nitrogen atom from the peptidic amide group might happen for a minor proportion of the Ag-GSH species.

This second anchoring for Ag-GSH would not interfere with the interpretation of an adsorbed Y-shaped GSH molecule (most probable structural configuration found for glutathione at acidic pH[66]), in which the carboxyl and amino groups are distanced from the vicinity of the thiol group, inhibiting deprotonation of these functional groups by interaction with the metal surface, but the amide group remains closer to the metal surface, even in a dense packing of mostly single anchored molecules.

3.1.3 Optical absorption. For core diameters of 2 nm and below, the surface/core metal atoms ratio significantly favors the surface atoms that belong to the core-ligand interface, thereby maximizing the effect that the ligand exerts on the geometric properties and electronic structure of the conjugated system, including metal–thiolate charge transfer.[44,116–119] This is reflected in the optical and chiroptical properties of the thiolate-functionalized metal nanoparticles under investigation, which will be analyzed through their respective UV-Vis absorption and circular dichroism spectra below.

The UV-Vis spectra shown in Fig. 4 correspond to L- (in blue) and D- (in red) glutathione-functionalized gold, silver and copper nanoparticles, namely Au-LGSH, Au-DGSH, Ag-LGSH, Ag-DGSH, Cu-LGSH and Cu-DGSH. The absorption spectra for each nanoparticle functionalized by either enantiomer of glutathione are similar, as expected, since absorption spectroscopy is not sensitive to chirality. Any slight variations in the spectra are primarily due to differences in the synthesis of each enantiomer of glutathione, resulting in different polymorphs with different solubilities for each enantiomer, as mentioned above.

Met-GSH NPs exhibit absorption bands between 230 and 400 nm for all three metals. Specifically, Au-GSH shows bands at 240, 275, 310 and 350 nm (5.16, 4.5, 3.99 and 3.54 eV); Ag-GSH has bands at 279 nm and 360 nm (4.44 and 3.44 eV); and Cu-GSH displays bands at 240 and 300 nm (5.16 and 4.13 eV). Consistent with previous results[20,41,44,45,47,80] there is no evidence of a strong surface plasmon resonance for this size of thiol-functionalized metal nanoparticles, responding to an intermediate regime between metallic and molecular behavior. This observation also aligns with the understanding that capping agents like glutathione act as modifiers of the electronic structure of nanoparticles, affecting their surface plasmon resonance by altering the oscillation frequency of the conduction band electrons at the surface.[109] Notably, absorption bands at 500 nm and above—typically associated with conventional thiolate-functionalized Au nanoclusters (NCs) containing more than 15 gold atoms[44,80,120–122]—were not detected for any of the metals. A possible hypothesis for this difference is that, opposite to the so-called gold thiolate-monolayer protected clusters (MPCs),[54] our conjugated system does not present a metal core completely isolated by a monolayer of adsorbates, but instead a partial coverage of GSH ligands in a non-closed core–shell fashion. In this scenario intermolecular interactions might be in competition with metal–ligand interactions, favouring the formation of supramolecular assemblies. However, our results also resemble previously reported Au(0)@Au(I) thiolate NCs with a metal : ligand ratio close to 1 : 1 demonstrated by ESI and TGA analysis,[80] which can be another complementary explanation for the lower energy limit of the obtained optical spectra.

In the case of Au-GSH (Fig. 4a), bands at higher energies (240 and 275 nm) are associated with the inter-band transitions from the Au–S bonding or Au 5d orbitals to the unoccupied Au 6s/6p orbitals, whereas bands at 310 and 350 nm have been assigned to the intra-band transitions from the high-lying occupied Au 6s orbitals to the low-lying unoccupied Au 6s/6p orbitals, this according to the optical spectra criterion, established by systematic theoretical studies, of localizing intraband transitions below 4 eV and interband transitions above this energy.[44]

The steplike behavior of the Au-GSH absorption spectrum in the energy region between 5.2 and 3.5 eV is evident, demonstrating discreteness of optical features that resemble previous results for size-separated Au-GSH nanoclusters obtained by PAGE electrophoresis[44,45] and by direct synthesis[6,48,65]

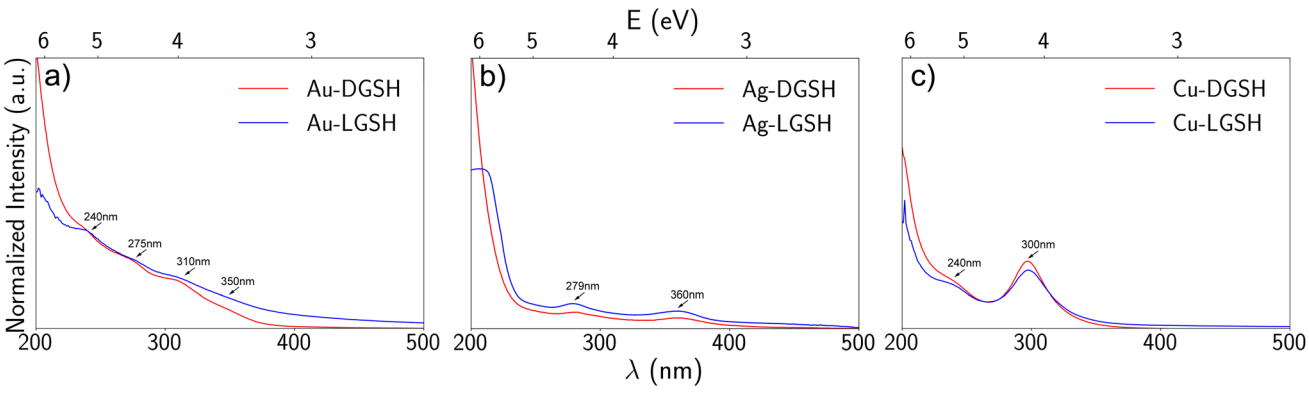

Fig. 4 Normalized absorption spectra of left (blue) and right (red) enantiomers of GSH-functionalized nanoparticles Au-D/LGSH (a); Ag-D/LGSH (b); and Cu-D/LGSH (c).

determined as $Au_{10}(SG)_{10}$, $Au_{11}(SG)_{11}$, $Au_{12}(SG)_{12}$ and $Au_{15}(SG)_{13}$ by electrospray ionization (ESI) mass spectrometry.

Based on this comparison, we can conclude that although microwave-assisted hydrolysis does not produce monodispersed thiol-functionalized gold nanoclusters (as evidenced by the broadness of the transition bands[53]), it effectively enables the direct and large-scale production of ultrasmall Au–thiolate nanoparticles with a narrow size distribution, all without the use of an extra reducing agent.

It is also important to note that our sample exhibits absorption between 300–400 nm, which safely rules out the possibility of solely being in the presence of an Au(I)–thiolate polymer, as its lowest absorption appears below 300 nm.[41,44] However, we cannot exclude the presence of other cyclic structures, corresponding to $Au_{10-12}(SG)_{10-12}$ that intercalate gold and sulfur atoms in a 1 : 1 ratio which have shown similar absorption spectra.[65,67]

The absorption spectra of silver (Ag) and copper (Cu), were also examined. The absorption spectrum for Ag-GSH NPs, shown in Fig. 4b, is the only one out of the three Met-GSH NPs that closely resembles that of cysteine-functionalized nanoparticles (Ag-Cys NPs in this case) synthesized under similar conditions. Both spectra exhibit bands at 278 nm and 359 nm.[71] Finally, Cu-GSH (Fig. 4c) shows a defined band at 300 nm and a weaker band at 240 nm, in agreement with previous results reported for similar synthesis methods in which glutathione is used not only as a capping agent but also as a reducing agent.[9,123–125]

In all cases, the optical onset is displaced from 5.2 eV corresponding to glutathione, to lower energies, indicating a larger optical gap as a result of the hybridization of the electronic orbitals of nanoparticle and molecular modifier. This behavior is also observed in the optical activity of each GSH-functionalized different metal nanoparticle as described below.

3.1.4 Chiroptical absorption. Left and right enantiomers of glutathione show mirror circular dichroism signals below 260 nm (Fig. 5a). It is worth noting that the CD signals of glutathione enantiomers are inverted respect to cysteine (Fig. 5b), *i.e.* in the case of cysteine the left enantiomer has positive signal and the right enantiomer negative mirror signal, in contrast to glutathione which presents a negative signal for its left enantiomer and positive for the right one. Cysteine only has one chiral center at the alpha carbon (Fig. 5d), whereas glutathione, a tripeptide constituted by three amino acids, has two chiral centers, one corresponding to the alpha carbon of cysteine, the middle amino acid, and the other corresponding to the alpha carbon of glutamic acid (the third amino acid, glycine, is achiral) (Fig. 5c).

Fig. 6 shows the circular dichroism spectra corresponding to L- (in blue) and D- (in red) glutathione-functionalized gold, silver and copper nanoparticles. All three metals exhibit distinct optical activity in the wavelength range of 250 to 450 nm. In the case of gold, we again disregard the Au-GSH polymer, which has been reported to be inactive beyond 300 nm. The strong optical activity results in high anisotropy factors (rarely exceeding 4×10^{-3} for systems with ligand-induced chirality[126,127]), particularly for the case of Ag-GSH, which reaches 5×10^{-3} (Fig. S5†).

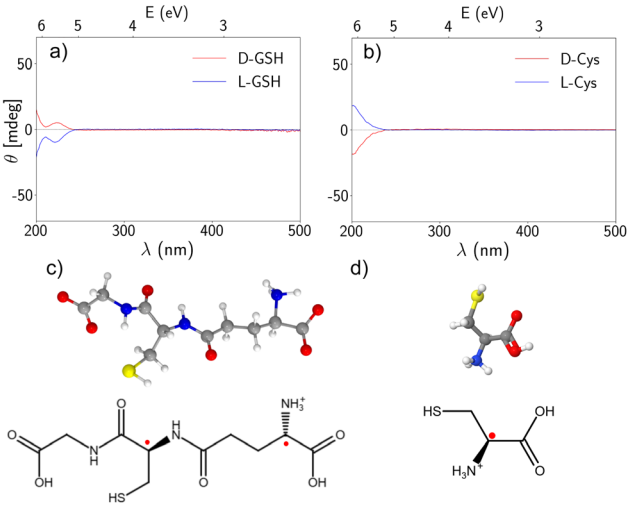

Fig. 5 Circular dichroism spectra of left (blue) and right (red) glutathione (a) and cysteine (b). Structural formula along with 3D representation of L-GSH (c) and L-Cys (d). Marked with asterisk two stereogenic centers in glutathione, as opposed to only one in cysteine.

This activity includes features that correspond to the mixing of the chiral ligand's orbitals with those of the metal nanoparticle.[60] The CD spectra differ unambiguously from the spectra corresponding to the ligand pre-adsorption, indicating a metal electronic structure that reacts to the chiral environment imposed by the molecular adsorbates, displaying different results determined by the nature of the metal and the molecular chain of the ligand. The opposite sign and mirror optical activity displayed in the metal-based electronic transitions for each one of the hybrid complexes, depending on the corresponding left or right adsorbed glutathione enantiomer, demonstrates that all of them have well-defined stereo-structures.[128] Spectral chiroptical features are evident for all three metals, displaying positive and negative Cotton effects for right and left enantiomers. These features exhibit nearly perfect mirror symmetry between the enantiomers, with slight variations in intensity likely attributable to differences in synthesis methods that result in slightly different crystalline structures for each enantiomer. In all three cases, these effects are dominated by interband transitions, which will be discussed in detail below.

Au-DGSH CD spectrum (Fig. 6a in blue) shows a negative band at 220 nm as the contribution from the adsorbate groups in the deep ultraviolet region, which is delimited to $E \geq 5$ eV for glutathione (Fig. 5a). It is worth noting that free D-GSH exhibits a positive CD band at that precise wavelength (Fig. 5a), which inverts to negative upon conjugation with Au NPs, opposite to what is observed in cysteine-functionalized Au NPs, where the sign of free cysteine bands is preserved for Au-Cys NPs in that energy region (both positive for the left enantiomer)[71] (Fig. S3a and d†). From 5 eV to lower energies it is possible to observe intercalated positive and negative bands at 231, 250, 300, 348 and 383 nm (5.36 eV, 4.95 eV, 4.13 eV, 3.56 eV, 3.23 eV respectively). This CD spectrum also resembles previous results of

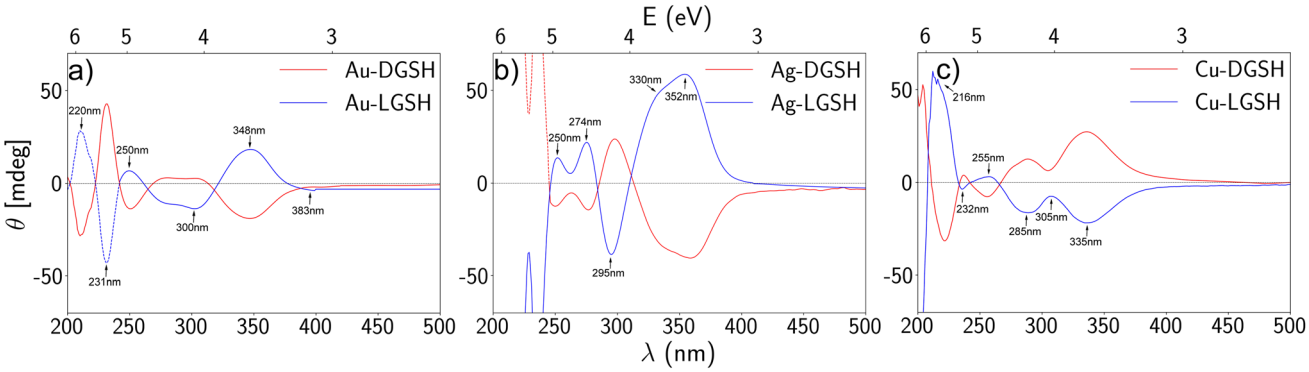

Fig. 6 Circular dichroism spectra of left (blue) and right (red) enantiomers of GSH-functionalized nanoparticles Au-D/LGSH (a); Ag-D/LGSH (b); and Cu-D/LGSH (c) nanoparticles. The dashed spectra represent the mirror image of the opposite enantiomer completed *a posteriori* for segments at energies near 6 eV with low signal-to-noise ratio.

ultrasmall glutathione-functionalized Au clusters for higher energies, matching the chiroptical features between 6 eV and 3 eV, but lacking such behavior towards lower energies.[3,4,41,47,129] The Au-GSH CD spectrum also aligns with recent findings for $Au_{10}(SG)_{10}$, which has been identified as a catenane nanocluster made up of two interconnected $Au_5(SG)_5$ rings with a centrosymmetry-broken structure. This structure exhibits an enhanced second harmonic response, suggesting that the presence of chiral Au-GSH ultrasmall complexes cannot be ruled out.[65]

Under the light of such similarities and contrasting with our TEM images, it can be said that by microwave assisted hydrolysis it is possible to produce a size distribution that includes 2 nm metal nanoparticles functionalized by glutathione (easily identifiable by electron microscopy), whose interface dominates the absorption profile observed in our measurements, and a fraction of ultrasmall glutathione–Au clusters, with cyclic gold–thiol structures, and no core–shell structure,[58,65,79,130] which have a distinctive electronic and optical behavior apart from the Au(I)–thiolate polymeric complexes.

There is not an exhaustive body of results regarding glutathione-functionalized silver nanoparticles; however, we can compare our circular dichroism (CD) spectrum with previous findings.[12,24,78,131] In all cases, the reported bands appear at wavelengths between 200 and 400 nm, which are similar to those we identified. Our results include a high-intensity negative band at 225 nm (this band is out of scale in Fig. 6b), a positive doublet at 250 and 274 nm, a negative band at 295 nm, and a broad positive band with a shoulder at 330 and 352 nm (5.51 eV, 4.95 eV, 4.52 eV, 4.20 eV, 3.75 eV, 3.52 eV respectively).

Ag-GSH shows significant similarity to Ag-Cys[71] (Fig. S3b and e†), in alignment with their respective absorption spectra (see Fig. 4), although there is an important difference: the spectral features of the left enantiomer of cysteine-functionalized silver nanoparticles closely resemble those of the right enantiomer of glutathione-functionalized silver nanoparticles in terms of wavelength, intensity, and even shape, and *vice versa*.

In order to explain such behavior we should bear in mind that the chiroptical properties of our systems are strongly dependent on the stereochemistry of the surface ligands. In this way, the sign of a Cotton effect is mainly dictated by the absolute configuration of the nearest stereogenic center to the corresponding absorption band.[132] Now, while cysteine is an amino acid with one chiral center (one stereogenic carbon), glutathione is a tripeptide with two chiral amino acids, cysteine and glutamic acid (the third amino acid, glycine, is achiral), therefore having four possible stereoisomers (LL, LD, DL and DD) and consequently two chiral centers (Fig. 5b). Considering the above, the observed inversion of optical activity for the silver nanoparticles with these two left ligands can be attributed to the L-glutathione stereoisomer (γ-L-glutamyl-L-cysteinyl-glycine) having a global stereogenic configuration opposite to L-cysteine.[78]

It is worth mentioning that Ag-GSH NPs presented the highest anisotropy factor (5×10^{-3}) among the three different metal NPs (Fig. S5†), which is possibly related to the second anchoring site through the nitrogen atom from the amide group as evidenced by XPS in a small proportion. This hypothesis is based on previous findings that point to a stronger optical activity resulting from bidentate adsorption configurations.[128]

With regard to copper, Cu-GSH NPs have been extensively studied but not in terms of their chirality. In fact, it is our understanding that the chiroptical results here reported are without precedent, showing a CD spectrum for Cu-GSH NPs with intercalated positive and negative bands at 216, 232, 255, 285, 305 and 335 nm (5.74 eV, 5.34 eV, 4.86 eV, 4.35 eV, 4.06 eV, 3.70 eV respectively) for the left enantiomer. A recent work[133] reports the CD spectra of L/D-GSH stabilized Cu NCs with diameter around 2.8 nm, but showing signal only between 300 and 400 nm, range in which their spectra are in agreement with our results.

The observed bands are in strong similarity with previous CD results of cysteine-functionalized copper NPs (Cu-Cys NPs) synthesized with the same methodology[71] (Fig. S6c and f†), suggesting that in the case of copper, the molecular chain of the ligand exerts the minimum influence on the overall chiroptical activity among the three metals. The same correlation can be carried out with the CD spectra of cysteine capped copper nanoclusters $(D/L\text{-Cys})_2Cu_4I_4$ with iodine acting as an electron

donating center,[134] a small system that was used to demonstrate that the chirality of the clusters highly depends on the direction of ligand arrangement around the CuI core.

Even though all Cu-GSH bands are bounded by the same limits as Au-GSH and Ag-GSH, among the three metal nanoparticles, Cu-GSH showed the onset with minimum energy at 2.6 eV, compared with Ag-GSH onset at 2.75 eV and Au-GSH onset at 2.9 eV.

Circular dichroism has been used to differentiate between structural conformation of GSH on Au and Ag NPs,[81] focusing on the region between 190 nm and 250 nm. This wavelength range was analyzed based on the consideration that CD spectra always display a positive band between 195 and 210 nm and a negative band between 215 and 230 nm for beta-sheet structures.[135] Our measurements show slight differences between Au-GSH and Ag-GSH in the 200–230 nm spectral region: while Au-GSH only shows one inflection point at 223 nm, with positive and then negative CD signal, Ag-GSH displays two inflections at 205 nm and 215 nm, going from negative to positive and then negative ellipticity again. On the other hand, Cu-GSH only displays one inflection point but at 210 nm, with a positive band occupying most of the analyzed range. Realizing a similar comparative analysis, and contrasting with our FTIR results, it can be suggested that a glutathione supramolecular structure, possibly built by hydrogen bonding between carboxylate and amine groups as it has been proposed before,[27,28,66] could be facilitated by all three metal nanoparticles, adopting similar arrays for gold and silver NPs, and a different configuration for copper NPs.

In general, it has been found that differences in the chiroptical properties of the three glutathione-functionalized metal nanoparticles are dictated by the interaction mechanisms happening at the metal–ligand interface; and differences observed with respect to metal nanoparticles functionalized with cysteine are determined by the stereochemistry of the surface ligands.[11] To gain further insight into these mechanisms, we performed time-dependent DFT calculations using an interface model for a single element of the aforementioned interface in the chiral system.

3.2 Theoretical calculations

As discussed previously, the CD signals observed within the 200 to 400 nm wavelength range indicate that the spectra predominantly reflect interface chiroptical activity.[43] The monomeric SR-Au-SR staple motif has been proposed as a prototype of the interface in ligand-functionalized metal clusters.[136,137] This structural unit has been observed using scanning tunneling microscopy and X-ray single-crystal techniques for self-assembled monolayers on gold nanoparticles.[138,139] When ligand coverage is low, staples can be arranged in a *cis–trans* pattern on the nanoparticle surface.[137] Jiang *et al.* performed DFT calculations on the thiolate-protected Au_{38} cluster and found that the staple motif is the most stable structure.[140] Additionally, this model was employed to elucidate the chiroptical activity of cysteine-protected metal nanoparticles, wherein the predominant transitions were identified as ligand-to-metal charge transfer (LMCT).[71] The staple motif was employed as a model for the glutathione-protected metal nanoparticle interface (Fig. 7). Based on previous reports on the Au-GSH structure, several conformations of the ligand were explored.[50] The structural analysis of the optimized models shows that modifying the metal in the monomeric staple model leads to minor changes in structure, mainly influencing sulfur–metal distances and non-covalent interactions of the ligand chain (Fig. S7†).

Time-dependent density functional theory (TD-DFT) calculations were conducted to provide further insights into the CD spectra of the Au-GSH, Ag-GSH, and Cu-GSH systems. The calculated CD and UV-Vis absorption spectra were divided into four color regions, namely yellow, cyan, magenta, and green (Fig. 8). The regions were colored in accordance with the sign changes of the rotatory strength. In certain instances, the maximum intensity observed in the absorption spectrum is indicative of a change in sign in the CD spectrum. This phenomenon can be observed, for example, in the absorption band at 310 nm in the spectrum of the Ag-GSH model. The position and amplitude of the Cotton effect are unique characteristics of each chiral system, resulting from the presence of chromophores that exhibit $n \rightarrow \pi^*$ and $\pi \rightarrow \pi^*$ transitions.[141,142] In consequence, the CD spectra of the Au-GSH, Ag-GSH, and Cu-GSH systems evince notable similarities, given that the chromophore groups are identical. However, the effect of the metal is represented as a shift to lower wavelengths in both the green and magenta regions, where the Cu-GSH system exhibits a shift of approximately 50 nm compared to the Au-GSH system. The results for Au and Ag are more analogous to those for Cu, given that these metals possess comparable atomic radii.[139] Finally, a comparison of the theoretical and experimental CD spectra of Au-GSH, Ag-GSH, and Cu-GSH shows a satisfactory level of agreement between them (Fig. S8†).

The electron transitions exhibiting the highest rotatory strength were selected. The transition density $T(r)$ reveals the region of the electron–hole coherence of an excitation.[95] A comparative analysis of the $T(r)$ isosurface maps for the Au-GSH, Ag-GSH, and Cu-GSH models reveals similarities (Fig. S9–S11 in the ESI†). The green, magenta, and cyan regions, which span the wavelength range from 260 to 400 nm, are indicative of a $T(r)$ distribution in the metal and sulfur atoms. In

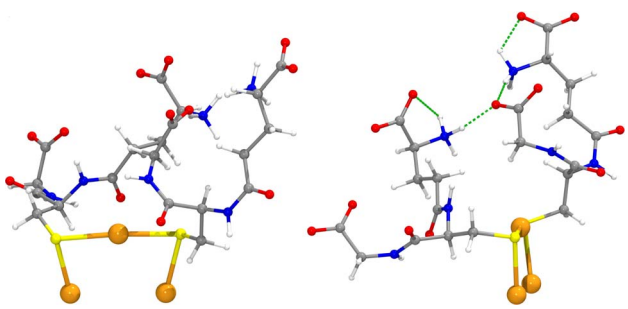

Fig. 7 Interface motif model of Au-GSH (front and side views are displayed). Color codes: Au = orange, S = yellow, C = gray, O = red, N = blue, and H = white.

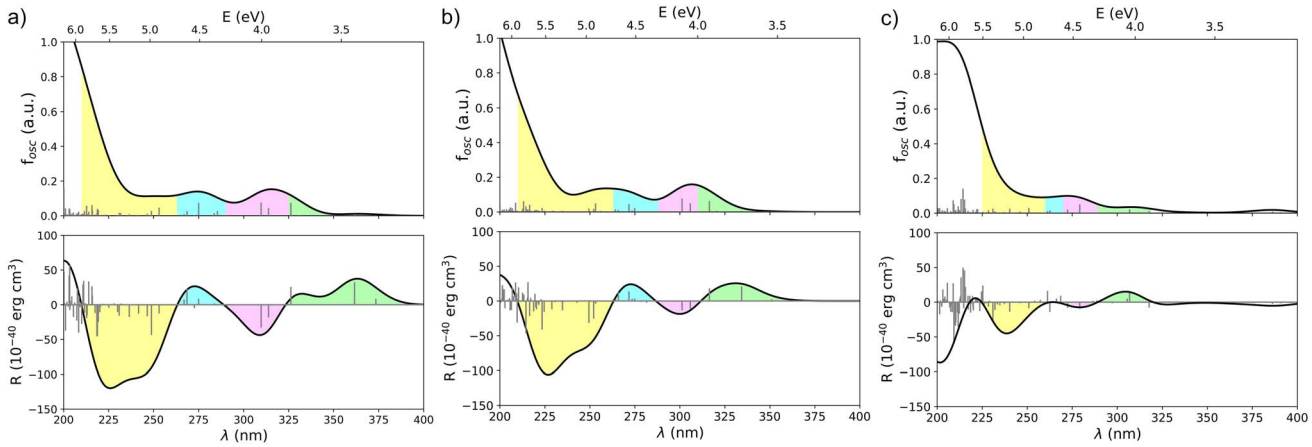

Fig. 8 Effect of metal on the UV-Vis absorption (top panel) and circular dichroism (CD) spectra (bottom panel) for interface motifs. (a) Au-GSH, (b) Ag-GSH, (c) Cu-GSH. The spectra are divided into four distinct zones, each identified with a different color, which correspond to the CD signals.

contrast, the yellow region (210 to 260 nm) demonstrates a more diverse contribution of the structure, with $T(r)$ distributed at the metal atoms and the chromophore groups of cysteine and glycine.

Furthermore, an analysis of natural transition orbitals (NTOs) was conducted for the most significant excitations of the Au-GSH interface model (Fig. 9). NTOs are typically more convenient than canonical Kohn–Sham orbitals, especially when many amplitudes are involved in a transition.[95] In the green region, the two transitions with the highest rotatory strength (3.43 and 3.80 eV) consist of a donor orbital (hole) situated in the Au–S staple and an acceptor orbital (electron) primarily located in the metal atoms. In the magenta region (3.95 and 4.00 eV), the hole isosurface is a π-type orbital of the glycine carboxylate and peptide bond, while the electron isosurface distribution is on Au atoms. These transitions can be described as ligand-to-metal charge transfer (LMCT). In the cyan region (4.50 and 4.62 eV), the hole orbital demonstrates a π-type contribution from the carboxylate groups of glycine and glutamate, while the electron orbital is associated with the Au–S interface. This behavior can also be described as a LMCT process. In the yellow region, electron transitions involving Au–S atoms are still observed at 5.24 eV. At higher energies, the ligand-to-ligand charge transfer (LLCT) process with a π-type

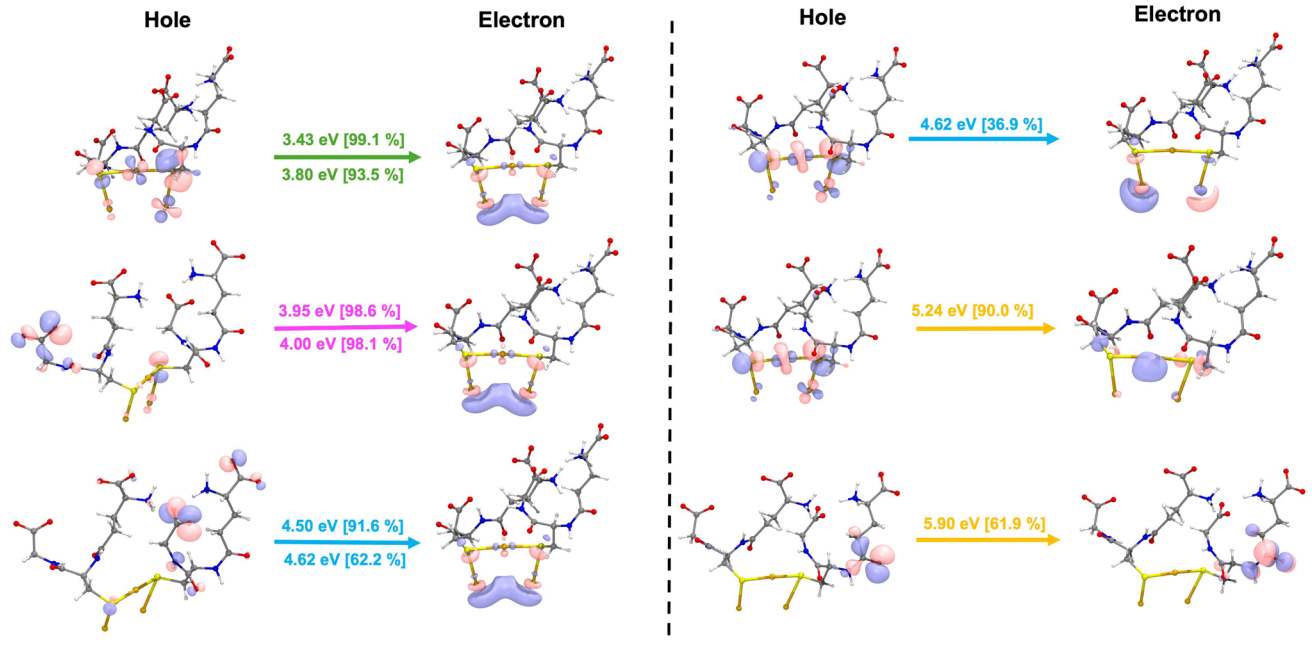

Fig. 9 Natural transition orbitals (NTOs) for electron transitions with the highest rotatory strength of the Au-GSH interface model. The amplitudes (in percentage) and energies (in eV) are displayed, with matching colors and arrows to the CD signals in Fig. 8. The phases of NTOs are represented in blue and pink with an isovalue of 0.05 a.u.

character is observed. A similar pattern is noted in the electron transitions of the Ag-GSH and Cu-GSH systems (Fig. S12 and S13†).

Overall, the staple motif provides a profile of the CD spectrum similar to the experiment. This model is responsible for the CD signals between 260 and 400 nm. The effect of the metal on the CD spectrum is a shift to lower wavelengths in the electronic transitions, especially when comparing the Au-GSH and Cu-GSH systems. The color-coded CD spectrum shows that LMCT excited states are primarily contributed by the Au and S atoms. In the magenta and cyan regions (260–325 nm), there are contributions from LMCT transitions where the ligand orbitals are π-type (from carboxylate groups and peptide bond). Finally, ligand-to-ligand charge transfer (more precisely $\pi \rightarrow \pi^*$ transitions) occur at about 210 nm in the spectrum.

4 Conclusions

Here, gold, silver, and copper nanoparticles were synthesized by a green and facile method and functionalized with left and right glutathione enantiomers (L-GSH and D-GSH, respectively) to explore the mechanisms of chirality transfer observed by the emergent optical activity in the three cases. The three different bare metal nanoparticles, originally achiral, exhibited circular dichroism signal upon ligand conjugation, with peaks at wavelengths above 230 nm (maximum wavelength for free glutathione), displaying mirror spectra for each Met-GSH enantiomer, and below 400 nm, in contrast to the so-called gold thiolate-monolayer protected clusters (MPCs). The energy range that shows signal (2.6–6 eV) indicates that the observed chiroptical activity is reigned in all three cases by the metal–ligand interface. This hypothesis was supported by TD-DFT calculations using as model an interface motif which delivered spectra in qualitative agreement with the experimental results. Additionally, it was determined that the majority of transitions observed in the CD spectrum involve metal and S atoms through LMCT excited states. Some transitions involving the ligand comprise groups with π electrons, including carboxylate and peptide bonds.

In a comparison of the optical and chiroptical properties observed for Met-GSH NPs with well-studied MPCs, we found that our GSH-functionalized NPs bare resemblance in optical absorption and circular dichroism ellipticity to well-defined closed shell structures in the UV energy regime but consistently differ for lower energies, lacking optical activity below 2.6 eV. This behaviour seems to be distinctive of the size regime in which our nanoparticles are found, an intermediate between GSH-protected nanoclusters and larger, plasmonic nanoparticles, and might be a consequence of a partial coverage of the metal core by the molecular adsorbates related to a variation from the conventional metal : ligand ratios.

In contrast to previously reported nanoparticles of the same size functionalized with cysteine,[71] Met-GSH NPs showed variations originating from the two adjacent amino acids that constitute the tripeptide, demonstrating that for this size regime, differences in the molecular chain of thiolate ligands result in differences in chiroptical behavior (particularly inversion of optical activity for silver NPs), contrary to what has been observed for clusters protected by thiolate monolayers. Variations among Met-GSH CD spectra are attributed to the subtle differences in adsorption configuration of the ligand in the three different metal surfaces, evidenced by XPS and FTIR spectra: Ag-GSH NPs showed a low-proportion second anchoring site through the nitrogen atom of the amide group, which is located in proximity to the thiol group (first anchoring point for all three Met-GSH NPs) and therefore does not interfere with densely packing of Y-shaped glutathione molecules on the silver surface. Such bidentate anchoring, although in a small proportion, could be partially the reason behind the higher anisotropy factor displayed by Ag-GSH NPs.

Copper nanoparticles presented a similar response to functionalization with GSH than Au NPs, confirming recent findings that copper competes with gold in stability for metal–thiolated interactions.

Metal–ligand interactions also determine the supramolecular hydrogen bonding assembly, which in turn defines the overall chiroptical response of each conjugated system. The exact structure of such a network was not concluded and it is material for future work, although FTIR and CD results combined suggests that a beta-sheet kind of array cannot be discarded.

The optical properties of coinage metal nanoparticles in interaction with their environment makes them appealing for chirality-related sensing applications.[8] On the other hand, glutathione is a chiral tripeptide with multiple physiological functions. Combined, Met-GSH NPs present synergistic properties that merit detailed exploration. Attainment of a fully understanding of glutathione-metal nanoparticles diverse conjugated systems paves the way for tailoring their chiroptical properties as well as other structural properties that are intrinsically related with their chirality, and in this manner to achieve better performance in applications such as chiral biomedicine.

Data availability

The authors confirm that the data supporting the findings of this study are available within the article and the ESI.†

Author contributions

J. C. López-Olivos: investigation, data curation, formal analysis, validation, visualisation; A. Álvarez-García: formal analysis, validation, visualisation, writing – review and editing; G. Garza Ramos: investigation; L. Huerta: investigation, formal analysis; P. Molina: investigation; A. Heredia-Barbero: resources, funding acquisition; I. L. Garzón: conceptualization, supervision, writing – review and editing; P. Rodríguez-Zamora: conceptualization, resources, investigation, formal analysis, writing – original draft, writing – review and editing.

Conflicts of interest

There are no conflicts to declare.

Acknowledgements

This work was supported by DGAPA-UNAM under project IA102825. JCLO gratefully thanks CONAHCyT-Mexico for the Master Scholarship. AAG gratefully thanks CONAHCyT-Mexico for the PhD scholarship no. 957574. The authors extend their heartfelt gratitude to Carlos Ernesto López Natarén for his invaluable assistance with the high-performance computing infrastructure used to perform our calculations, as well as for his unwavering support throughout the project. Special thanks are also extended to Luis Fernando Garrido-García for his expertise and support with FTIR analysis, Cristina Zorrilla and Claudia C. Camargo Raya for their essential laboratory assistance, and Josué E. Romero-Ibarra and Roberto Hernández Reyes for their contributions to the TEM topographies acquisition. ILG was supported by PASPA-DGAPA-UNAM through a sabbatical fellowship at the Universidad de Valladolid, Spain. ILG also acknowledges the hospitality of the Departamento de Física Teórica, Atómica y Óptica de la Facultad de Ciencias de la Universidad de Valladolid, Spain, during a sabbatical year.

References

1 S. Bettini, M. Ottolini, D. Valli, R. Pagano, C. Ingrosso, M. Roeffaers, J. Hofkens, L. Valli and G. Giancane, *Nanomaterials*, 2023, **13**(9), 1526.
2 L. A. Warning, A. R. Miandashti, L. A. McCarthy, Q. Zhang, C. F. Landes and S. Link, *ACS Nano*, 2021, **15**, 15538–15566.
3 S. Kumar and R. Jin, *Nanoscale*, 2012, **4**, 4222–4227.
4 J. Liu, P. N. Duchesne, M. Yu, X. Jiang, X. Ning, R. D. Vinluan III, P. Zhang and J. Zheng, *Angew. Chem., Int. Ed.*, 2016, **55**, 8894–8898.
5 M. Pourmbarak Mahnaie and H. Mahmoudi, *Eur. J. Med. Res.*, 2020, **25**, 17.
6 K. G. Stamplecoskie and P. V. Kamat, *J. Am. Chem. Soc.*, 2014, **136**, 11093–11099.
7 H. Häkkinen, *Nat. Chem.*, 2012, **4**, 443–455.
8 M. Jakob, A. von Weber, A. Kartouzian and U. Heiz, *Phys. Chem. Chem. Phys.*, 2018, **20**, 20347–20351.
9 X. Gao, J. Liu, X. Zhuang, C. Tian, F. Luan, H. Liu and Y. Xiong, *Sens. Actuators, B*, 2020, **308**, 127720.
10 K. Klein, K. Loza, M. Heggen and M. Epple, *ChemNanoMat*, 2021, **7**, 1330–1339.
11 L.-S. Wagner, O. Prymak, T. Schaller, C. Beuck, K. Loza, F. Niemeyer, N. Gumbiowski, K. Kostka, P. Bayer, M. Heggen, C. L. P. Oliveira and M. Epple, *J. Phys. Chem. B*, 2024, **128**, 4266–4281.
12 A. Ghosh, A. K. Prasad and L. Chuntonov, *J. Phys. Chem. Lett.*, 2019, **10**, 2481–2486.
13 J. C. Azcárate, G. Corthey, E. Pensa, C. Vericat, M. H. Fonticelli, R. C. Salvarezza and P. Carro, *J. Phys. Chem. Lett.*, 2013, **4**, 3127–3138.
14 R. Subbiah, M. Veerapandian and K. S. Yun, *Curr. Med. Chem.*, 2010, **17**, 4559–4577.
15 G. Sanità, B. Carrese and A. Lamberti, *Front. Mol. Biosci.*, 2020, **7**, 1–20.
16 X. Yuan, Y. Tay, X. Dou, Z. Luo, D. T. Leong and J. Xie, *Anal. Chem.*, 2013, **85**, 1913–1919.
17 Y. Qi, M. Xu, H. Lu, X. Wang, Y. Peng, Z. Wang, F. Liang, X. Jiang and B. Du, *Angew. Chem., Int. Ed.*, 2024, **63**, e202409477.
18 A. A. Sousa, S. A. Hassan, L. L. Knittel, A. Balbo, M. A. Aronova, P. H. Brown, P. Schuck and R. D. Leapman, *Nanoscale*, 2016, **8**, 6577–6588.
19 M. Sahu, M. Ganguly and A. Doi, *J. Cluster Sci.*, 2024, **35**, 1667–1685.
20 C. Wang, L. Ling, Y. Yao and Q. Song, *Nano Res.*, 2015, **8**, 1975–1986.
21 S. Uhlig and A. Wendel, *Life Sci.*, 1992, **51**, 1083–1094.
22 J. C. Luque-Ceballos, P. Rodríguez-Zamora, J. C. López-Olivos and I. L. Garzón, *Comput. Theor. Chem.*, 2023, **1227**, 114227.
23 L. L. Knittel, H. Zhao, A. Nguyen, A. Miranda, P. Schuck and A. A. Sousa, *J. Phys. Chem. B*, 2020, **124**, 3892–3902.
24 C. Zhang, K. Wang, C. Li, Y. Liu, H. Fu, F. Pan and D. Cui, *J. Mater. Chem. B*, 2014, **2**, 6931–6938.
25 Y.-T. Zhou, W. He, Y. M. Lo, X. Hu, X. Wu and J.-J. Yin, *J. Agric. Food Chem.*, 2013, **61**, 7855–7862.
26 S. Tang, Y. Huang and J. Zheng, *Angew. Chem., Int. Ed.*, 2020, **59**, 19894–19898.
27 M. R. Hormozi-Nezhad, E. Seyedhosseini and H. Robatjazi, *Sci. Iran.*, 2012, **19**, 958–963.
28 I.-I. S. Lim, D. Mott, W. Ip, P. N. Njoki, Y. Pan, S. Zhou and C.-J. Zhong, *Langmuir*, 2008, **24**, 8857–8863.
29 C. Zhang, Z. Zhou, X. Zhi, Y. Ma, K. Wang, Y. Wang, Y. Zhang, H. Fu, W. Jin, F. Pan and D. Cui, *Theranostics*, 2015, **5**, 134–149.
30 N.-N. Zhang, H.-R. Sun, Y. Xue, F. Peng and K. Liu, *J. Phys. Chem. C*, 2021, **125**, 10708–10715.
31 J. Lu, Y.-X. Chang, N.-N. Zhang, Y. Wei, A.-J. Li, J. Tai, Y. Xue, Z.-Y. Wang, Y. Yang, L. Zhao, Z.-Y. Lu and K. Liu, *ACS Nano*, 2017, **11**, 3463–3475.
32 B. Shi, J. Zhao, Z. Xu, C. Chen, L. Xu, C. Xu, M. Sun and H. Kuang, *Adv. Sci.*, 2022, **9**, 2202475.
33 R. Wei, X. Gao, Z. Cao, J. Wang and Y. Ma, *Biomimetics*, 2022, **7**, 1–13.
34 L. Xu, X. Wang, W. Wang, M. Sun, W. J. Choi, J.-Y. Kim, C. Hao, S. Li, A. Qu, M. Lu, X. Wu, F. M. Colombari, W. R. Gomes, A. L. Blanco, A. F. de Moura, X. Guo, H. Kuang, N. A. Kotov and C. Xu, *Nature*, 2022, **601**, 366–373.
35 A. Hooftman and L. A. J. O'Neill, *Nature*, 2022, **601**, 323–325.
36 Y. Wang and T. Bürgi, *Nanoscale Adv.*, 2021, **3**, 2710–2727.
37 K. Hou, J. Zhao, H. Wang, B. Li, K. Li, X. Shi, K. Wan, J. Ai, J. Lv, D. Wang, Q. Huang, H. Wang, Q. Cao, S. Liu and Z. Tang, *Nat. Commun.*, 2020, **11**, 4790.
38 C. Hao, A. Qu, L. Xu, M. Sun, H. Zhang, C. Xu and H. Kuang, *J. Am. Chem. Soc.*, 2019, **141**, 1091–1099.
39 P. Wang, L. Xiong, X. Sun, Z. Ma and Y. Pei, *Nanoscale*, 2018, **10**, 3918–3929.
40 T. G. Schaaff, G. Knight, M. N. Shafigullin, R. F. Borkman and R. L. Whetten, *J. Phys. Chem. B*, 1998, **102**, 10643–10646.
41 T. G. Schaaff and R. L. Whetten, *J. Phys. Chem. B*, 2000, **104**, 2630–2641.

42 C. Noguez and I. L. Garzón, *Chem. Soc. Rev.*, 2009, **38**, 757–771.
43 C. Zeng and R. Jin, *Chem.–Asian J.*, 2017, **12**, 1839–1850.
44 Y. Negishi, K. Nobusada and T. Tsukuda, *J. Am. Chem. Soc.*, 2005, **127**, 5261–5270.
45 Y. Shichibu, Y. Negishi, H. Tsunoyama, M. Kanehara, T. Teranishi and T. Tsukuda, *Small*, 2007, **3**, 835–839.
46 E. S. Shibu, M. A. H. Muhammed, T. Tsukuda and T. Pradeep, *J. Phys. Chem. C*, 2008, **112**, 12168–12176.
47 Z. Wu, J. Suhan and R. Jin, *J. Mater. Chem.*, 2009, **19**, 622–626.
48 Y. Yu, X. Chen, Q. Yao, Y. Yu, N. Yan and J. Xie, *Chem. Mater.*, 2013, **25**, 946–952.
49 C. M. Aikens, *J. Phys. Chem. C*, 2008, **112**, 19797–19800.
50 M. Monti, M. F. Matus, S. Malola, A. Fortunelli, M. Aschi, M. Stener and H. Häkkinen, *ACS Nano*, 2023, **17**, 11481–11491.
51 B. Ni, M. Mychinko, S. Gómez-Graña, J. Morales-Vidal, M. Obelleiro-Liz, W. Heyvaert, D. Vila-Liarte, X. Zhuo, W. Albrecht, G. Zheng, G. González-Rubio, J. M. Taboada, F. Obelleiro, N. López, J. Pérez-Juste, I. Pastoriza-Santos, H. Cölfen, S. Bals and L. M. Liz-Marzán, *Adv. Mater.*, 2023, **35**, 2208299.
52 J. Wan, L. Sun, X. Sun, C. Liu, G. Yang, B. Zhang, Y. Tao, Y. Yang and Q. Zhang, *J. Am. Chem. Soc.*, 2024, **146**, 10640–10654.
53 O. Bakr, V. Amendola, C. Aikens, W. Wenseleers, R. Li, L. Dal Negro, G. Schatz and F. Stellacci, *Angew. Chem., Int. Ed.*, 2009, **48**, 5921–5926.
54 X. L. Guevel, O. Tagit, C. E. Rodríguez, V. Trouillet, M. Pernia Leal and N. Hildebrandt, *Nanoscale*, 2014, **6**, 8091–8099.
55 Y. Li, T. Higaki, X. Du and R. Jin, *Adv. Mater.*, 2020, **32**, 1905488.
56 S. Malola, P. Nieminen, A. Pihlajamäki, J. Hämäläinen, T. Kärkkäinen and H. Häkkinen, *Nat. Commun.*, 2019, **10**, 3973.
57 M. F. Matus and H. Häkkinen, *Nat. Rev. Mater.*, 2023, **8**, 372–389.
58 D. M. Chevrier, L. Raich, C. Rovira, A. Das, Z. Luo, Q. Yao, A. Chatt, J. Xie, R. Jin, J. Akola and P. Zhang, *J. Am. Chem. Soc.*, 2018, **140**, 15430–15436.
59 J. Bhamore, K. A. Rawat, H. Basu, R. K. Singhal and S. K. Kailasa, *Sens. Actuators, B*, 2015, **212**, 526–535.
60 V. Truttmann, A. Loxha, R. Banu, E. Pittenauer, S. Malola, M. F. Matus, Y. Wang, E. A. Ploetz, G. Rupprechter, T. Bürgi, H. Häkkinen, C. Aikens and N. Barrabés, *ACS Nano*, 2023, **17**, 20376–20386.
61 A. Das, C. Liu, H. Y. Byun, K. Nobusada, S. Zhao, N. Rosi and R. Jin, *Angew. Chem., Int. Ed.*, 2015, **54**, 3140–3144.
62 X. Kang, H. Chong and M. Zhu, *Nanoscale*, 2018, **10**, 10758–10834.
63 M. Kamiyama, Y. Shingyouchi, R. Sarma, M. Ghosh, T. Kawawaki, S. Biswas and Y. Negishi, *Chem. Commun.*, 2025, **61**(6), 1048–1062.
64 Y. Negishi, N. K. Chaki, Y. Shichibu, R. L. Whetten and T. Tsukuda, *J. Am. Chem. Soc.*, 2007, **129**, 11322–11323.
65 F. Bertorelle, I. Russier-Antoine, N. Calin, C. Comby-Zerbino, A. Bensalah-Ledoux, S. Guy, P. Dugourd, P.-F. Brevet, Ž. Sanader, M. Krstić, V. Bonačić-Koutecký and R. Antoine, *J. Phys. Chem. Lett.*, 2017, **8**, 1979–1985.
66 M. Bieri and T. Bürgi, *Langmuir*, 2005, **21**, 1354–1363.
67 N. Kojima, Y. Kobayashi, Y. Negishi, M. Seto and T. Tsukuda, *Hyperfine Interact.*, 2013, **217**, 91–98.
68 Z. Luo, V. Nachammai, B. Zhang, N. Yan, D. T. Leong, D.-e. Jiang and J. Xie, *J. Am. Chem. Soc.*, 2014, **136**, 10577–10580.
69 A. Tlahuice and I. L. Garzón, *Phys. Chem. Chem. Phys.*, 2012, **14**, 3737–3740.
70 K. Nobusada and T. Iwasa, *J. Phys. Chem. C*, 2007, **111**, 14279–14282.
71 P. Rodríguez-Zamora, C. A. Cordero-Silis, G. R. Garza-Ramos, B. Salazar-Angeles, J. C. Luque-Ceballos, J. C. Fabila, F. Buendía, L. O. Paz-Borbón, G. Díaz and I. L. Garzón, *Small*, 2021, **17**, 2004288.
72 C. A. Bauer, F. Stellacci and J. W. Perry, *Top. Catal.*, 2008, **47**, 32–41.
73 K. A. Kacprzak, O. López-Acevedo, H. Hakkinen and H. Gronbeck, *J. Phys. Chem. C*, 2010, **114**(32), 13571–13576.
74 M. S. A. Hazer, S. Malola and H. Häkkinen, *Phys. Chem. Chem. Phys.*, 2024, **26**, 21954–21964.
75 I. Karki, H. Wang, N. R. Geise, B. W. Wilson, J. P. Lewis and T. Gullion, *J. Phys. Chem. B*, 2015, **119**, 11998–12006.
76 P. Rodríguez-Zamora, C. A. Cordero-Silis, J. Fabila, J. C. Luque-Ceballos, F. Buendía, A. Heredia-Barbero and I. L. Garzón, *Langmuir*, 2022, **38**, 5418–5427.
77 S. K. Balavandy, K. Shameli, D. R. B. A. Biak and Z. Z. Abidin, *Chem. Cent. J.*, 2014, **8**, 11.
78 N. Cathcart and V. Kitaev, *J. Phys. Chem. C*, 2010, **114**, 16010–16017.
79 C. Comby-Zerbino, F. Bertorelle, F. Chirot, P. Dugourd and R. Antoine, *Eur. Phys. J. D*, 2018, **72**, 144.
80 Z. Luo, X. Yuan, Y. Yu, Q. Zhang, D. T. Leong, J. Y. Lee and J. Xie, *J. Am. Chem. Soc.*, 2012, **134**, 16662–16670.
81 S. Chakrabarty, S. Maity, D. Yazhini and A. Ghosh, *Langmuir*, 2020, **36**, 11255–11261.
82 A. Baksi, M. S. Bootharaju, X. Chen, H. Häkkinen and T. Pradeep, *J. Phys. Chem. C*, 2014, **118**, 21722–21729.
83 C. Vargas-Hernandez, M. M. Mariscal, R. Esparza and M. J. Yacaman, *Appl. Phys. Lett.*, 2010, **96**, 213115.
84 M. Tsuji, *ChemistrySelect*, 2017, **2**, 805–819.
85 ULVAC-PHI, *MultiPak Data Reduction Software for XPS and AES*, 2010.
86 B. V. Crist, *Spectral Data Processor v4.1 (32 bit)*, 2004.
87 F. Neese, F. Wennmohs, U. Becker and C. Riplinger, *J. Chem. Phys.*, 2020, **152**, 224108.
88 F. Neese, *Wiley Interdiscip. Rev. Comput. Mol. Sci.*, 2022, **12**, e1606.
89 C. Adamo and V. Barone, *J. Chem. Phys.*, 1999, **110**, 6158–6170.
90 M. Ernzerhof and G. E. Scuseria, *J. Chem. Phys.*, 1999, **110**, 5029–5036.
91 A. Schäfer, C. Huber and R. Ahlrichs, *J. Chem. Phys.*, 1994, **100**, 5829–5835.

92 E. van Lenthe, J. G. Snijders and E. J. Baerends, *J. Chem. Phys.*, 1996, **105**, 6505–6516.
93 J. D. Rolfes, F. Neese and D. A. Pantazis, *J. Comput. Chem.*, 2020, **41**, 1842–1849.
94 V. Barone and M. Cossi, *J. Phys. Chem. A*, 1998, **102**, 1995–2001.
95 F. Plasser, M. Wormit and A. Dreuw, *J. Chem. Phys.*, 2014, **141**, 024106.
96 J. M. Herbert, *Phys. Chem. Chem. Phys.*, 2024, **26**, 3755–3794.
97 C. Zhou, G. Hao, P. Thomas, J. Liu, M. Yu, S. Sun, O. K. Öz, X. Sun and J. Zheng, *Angew. Chem., Int. Ed.*, 2012, **51**, 10118–10122.
98 C. Fernández-Ponce, J. M. Mánuel, R. Fernández-Cisnal, E. Félix, J. Beato-López, J. P. Muñoz-Miranda, A. M. Beltrán, A. J. Santos, F. M. Morales, M. P. Yeste, O. Bomati-Miguel, R. Litrán and F. García-Cózar, *Metals*, 2021, **11**, 1–23.
99 M. M. Alvarez, J. T. Khoury, T. G. Schaaff, M. Shafigullin, I. Vezmar and R. L. Whetten, *Chem. Phys. Lett.*, 1997, **266**, 91–98.
100 M. Miyoshi, K. Kotera, H. Seko, K. Masukawa, S. Imado and K. Okumur, *Bull. Chem. Soc. Jpn.*, 1969, **42**, 1749–1751.
101 J. Fu, F. Wang, Y. Shi, C. Wang, J. Zhao, Y. Hou, W. Zhuang, H. Ying, P. Yang and K. Zhang, *J. Mol. Liq.*, 2023, **386**, 122468.
102 R. M. Silverstein, F. X. Webster, D. J. Kiemle and D. L. Bryce, *Spectrometric Identification of Organic Compounds*, John Wiley & Sons, Chichester, England, 8th edn, 2014.
103 C. Fang and X. Zhou, *Electroanalysis*, 2003, **15**, 1632–1638.
104 A. Vallée, V. Humblot, C. Méthivier and C.-M. Pradier, *J. Phys. Chem. C*, 2009, **113**, 9336–9344.
105 F. Lobo Maza, L. Méndez De Leo, A. A. Rubert, P. Carro, R. C. Salvarezza and C. Vericat, *J. Phys. Chem. C*, 2016, **120**, 14597–14607.
106 C. P. Shaw, D. A. Middleton, M. Volk and R. Lévy, *ACS Nano*, 2012, **6**, 1416–1426.
107 H. S. Mandal and H.-B. Kraatz, *J. Am. Chem. Soc.*, 2007, **129**, 6356–6357.
108 J. P. Lomont, K. L. Rich, M. Maj, J.-J. Ho, J. S. Ostrander and M. T. Zanni, *J. Phys. Chem. B*, 2018, **122**, 144–153.
109 N. Wolff, K. Loza, M. Heggen, T. Schaller, F. Niemeyer, P. Bayer, C. Beuck, C. L. P. Oliveira, O. Prymak, C. Weidenthaler and M. Epple, *Inorg. Chem.*, 2023, **62**, 17470–17485.
110 O. Wetzel, S. Hosseini, K. Loza, M. Heggen, O. Prymak, P. Bayer, C. Beuck, T. Schaller, F. Niemeyer, C. Weidenthaler and M. Epple, *J. Phys. Chem. B*, 2021, **125**, 5645–5659.
111 X.-D. Zhang, Z. Luo, J. Chen, X. Shen, S. Song, Y. Sun, S. Fan, F. Fan, D. T. Leong and J. Xie, *Adv. Mater.*, 2014, **26**, 4565–4568.
112 K. Siow, L. Britcher, S. Kumar and H. Griesser, *Sains Malays.*, 2018, **47**, 1913–1922.
113 P. Yan, W. Zhao, F. McBride, D. Cai, J. Dale, V. Hanna and T. Hasell, *Nat. Commun.*, 2022, **13**, 4824.
114 J. Kettle, Z. Ding, M. Horie and G. Smith, *Org. Electron.*, 2016, **39**, 222–228.
115 P. Rodríguez-Zamora, B. Salazar-Angeles, F. Buendía, C. Cordero-Silis, J. Fabila, L. Bazán-Díaz, L. M. Fernández-Díaz, L. O. Paz-Borbón, G. Díaz and I. L. Garzón, *J. Raman Spectrosc.*, 2020, **51**, 243–255.
116 H. Häkkinen, R. N. Barnett and U. Landman, *Phys. Rev. Lett.*, 1999, **82**, 3264–3267.
117 I. L. Garzón, C. Rovira, K. Michaelian, M. R. Beltrán, P. Ordejón, J. Junquera, D. Sánchez-Portal, E. Artacho and J. M. Soler, *Phys. Rev. Lett.*, 2000, **85**, 5250–5251.
118 I. L. Garzón, J. A. Reyes-Nava, J. I. Rodríguez-Hernández, I. Sigal, M. R. Beltrán and K. Michaelian, *Phys. Rev. B: Condens. Matter Mater. Phys.*, 2002, **66**, 073403.
119 C. E. Román-Velázquez, C. Noguez and I. L. Garzón, *J. Phys. Chem. B*, 2003, **107**, 12035–12038.
120 K. Kimura, N. Sugimoto, S. Sato, H. Yao, Y. Negishi and T. Tsukuda, *J. Phys. Chem. C*, 2009, **113**, 14076–14082.
121 H. Qian and R. Jin, *Nano Lett.*, 2009, **9**, 4083–4087.
122 Y. Levi-Kalisman, P. D. Jadzinsky, N. Kalisman, H. Tsunoyama, T. Tsukuda, D. A. Bushnell and R. D. Kornberg, *J. Am. Chem. Soc.*, 2011, **133**, 2976–2982.
123 Y. Yang, Q. Wei, T. Zou, Y. Kong, L. Su, D. Ma and Y. Wang, *Sens. Actuators, B*, 2020, **321**, 128534.
124 M. Ye, Y. Yu, B. Lin, Y. Cai, Y. Cao, M. Guo and D. Zhu, *Sens. Actuators, B*, 2019, **284**, 36–44.
125 A. Baghdasaryan, R. Grillo, S. Roy Bhattacharya, M. Sharma, E. Reginato, H. Theraulaz, I. Dolamic, M. Dadras, S. Rudaz, E. Varesio and T. Burgi, *ACS Appl. Nano Mater.*, 2018, **1**, 4258–4267.
126 C. Gautier and T. Bürgi, *ChemPhysChem*, 2009, **10**, 483–492.
127 L. Francés-Soriano, E. Zaballos-García and J. Pérez-Prieto, *Adv. Opt. Mater.*, 2023, **11**, 2300337.
128 N. Nishida, H. Yao, T. Ueda, A. Sasaki and K. Kimura, *Chem. Mater.*, 2007, **19**, 2831–2841.
129 M. Zhu, H. Qian, X. Meng, S. Jin, Z. Wu and R. Jin, *Nano Lett.*, 2011, **11**, 3963–3969.
130 Q. Li, B. Huang, S. Yang, H. Zhang, J. Chai, Y. Pei and M. Zhu, *J. Am. Chem. Soc.*, 2021, **143**, 15224–15232.
131 T. Li, H. G. Park, H.-S. Lee and S.-H. Choi, *Nanotechnology*, 2004, **15**, S660.
132 J. T. Vázquez, *Tetrahedron: Asymmetry*, 2017, **28**, 1199–1211.
133 Q. Ding, W. Yang, X. Xing, H. Lin, C. Xu, L. Xu and S. Li, *Angew. Chem., Int. Ed.*, 2024, **63**, e202401032.
134 C. Dutta, S. Maniappan and J. Kumar, *Chem. Sci.*, 2023, **14**, 5593–5601.
135 N. J. Greenfield, *Nat. Protoc.*, 2006, **1**, 2876–2890.
136 P. D. Jadzinsky, G. Calero, C. J. Ackerson, D. A. Bushnell and R. D. Kornberg, *Science*, 2007, **318**, 430–433.
137 S. Knoppe and T. Burgi, *Acc. Chem. Res.*, 2014, **47**, 1318–1326.
138 O. Voznyy, J. J. Dubowski, J. T. Yates and P. Maksymovych, *J. Am. Chem. Soc.*, 2009, **131**, 12989–12993.
139 H. Häkkinen, *Nat. Chem.*, 2012, **4**, 443–455.
140 D. E. Jiang, M. L. Tiago, W. Luo and S. Dai, *J. Am. Chem. Soc.*, 2008, **130**, 2777–2779.
141 J. T. Vázquez, *Tetrahedron: Asymmetry*, 2017, **28**, 1199–1211.
142 N. Berova, L. D. Bari and G. Pescitelli, *Chem. Soc. Rev.*, 2007, **36**, 914–931.